ALCHEMI finds a "shocking" carbon footprint in the starburst galaxy NGC 253

Harada, N.; Martín, S.; Mangum, J.G.; Sakamoto, K.; Muller, S.; Rivilla, V.M.; ... ; Emig, K.L.

The Astrophysical Journal, 938:80 (15pp), 2022 October 10 https://doi.org/10.3847/1538-4357/ac8dfc

ALCHEMI Finds a "Shocking" Carbon Footprint in the Starburst Galaxy NGC 253

Nanase Harada[1,2], Sergio Martín[3,4], Jeffrey G. Mangum[5], Kazushi Sakamoto[6], Sebastien Muller[7], Víctor M. Rivilla[8], Christian Henkel[9,10,11], David S. Meier[12,13], Laura Colzi[8], Mitsuyoshi Yamagishi[14], Kunihiko Tanaka[15], Kouichiro Nakanishi[1,2], Rubén Herrero-Illana[3,16], Yuki Yoshimura[14], P. K. Humire[9], Rebeca Aladro[9], Paul P. van der Werf[17], and Kimberly L. Emig[5,18]

[1] National Astronomical Observatory of Japan, 2-21-1 Osawa, Mitaka, Tokyo 181-8588, Japan
[2] Department of Astronomy, School of Science, The Graduate University for Advanced Studies (SOKENDAI), 2-21-1 Osawa, Mitaka, Tokyo, 181-1855 Japan
[3] European Southern Observatory, Alonso de Córdova, 3107, Vitacura, Santiago 763-0355, Chile
[4] Joint ALMA Observatory, Alonso de Córdova, 3107, Vitacura, Santiago 763-0355, Chile
[5] National Radio Astronomy Observatory, 520 Edgemont Road, Charlottesville, VA, 22903-2475, USA
[6] Institute of Astronomy and Astrophysics, Academia Sinica, 11F of AS/NTU Astronomy-Mathematics Building, No.1, Sec. 4, Roosevelt Rd, Taipei 10617, Taiwan
[7] Department of Space, Earth and Environment, Chalmers University of Technology, Onsala Space Observatory, SE-439 92 Onsala, Sweden
[8] Centro de Astrobiología (CSIC-INTA), Ctra. de Ajalvir Km. 4, Torrejón de Ardoz, E-28850 Madrid, Spain
[9] Max-Planck-Institut für Radioastronomie, Auf dem Hügel 69, D-53121 Bonn, Germany
[10] Astronomy Department, Faculty of Science, King Abdulaziz University, P.O. Box 80203, Jeddah 21589, Saudi Arabia
[11] Xinjinag Astronomical Observatory, Chinese Academy of Sciences, 830011 Urumqi, People's Republic of China
[12] New Mexico Institute of Mining and Technology, 801 Leroy Place, Socorro, NM, 87801, USA
[13] National Radio Astronomy Observatory, PO Box O, 1003 Lopezville Road, Socorro, NM, 87801, USA
[14] Institute of Astronomy, Graduate School of Science, The University of Tokyo, 2-21-1 Osawa, Mitaka, Tokyo 181-0015, Japan
[15] Department of Physics, Faculty of Science and Technology, Keio University, 3-14-1 Hiyoshi, Yokohama, Kanagawa 223–8522 Japan
[16] Institute of Space Sciences (ICE, CSIC), Campus UAB, Carrer de Magrans, E-08193 Barcelona, Spain
[17] Leiden Observatory, Leiden University, PO Box 9513, NL-2300 RA Leiden, The Netherlands
Received 2022 June 22; revised 2022 August 9; accepted 2022 August 29; published 2022 October 14

Abstract

The centers of starburst galaxies may be characterized by a specific gas and ice chemistry due to their gas dynamics and the presence of various ice desorption mechanisms. This may result in a peculiar observable composition. We analyse the abundances of CO_2, a reliable tracer of ice chemistry, from data collected as part of the Atacama Large Millimeter/submillimeter Array large program ALCHEMI, a wide-frequency spectral scan toward the starburst galaxy NGC 253 with an angular resolution of 1.″6. We constrain the CO_2 abundances in the gas phase using its protonated form $HOCO^+$. The distribution of $HOCO^+$ is similar to that of methanol, which suggests that $HOCO^+$ is indeed produced from the protonation of CO_2 sublimated from ice. The $HOCO^+$ fractional abundances are found to be (1–2) $\times 10^{-9}$ at the outer part of the central molecular zone (CMZ), while they are lower ($\sim 10^{-10}$) near the kinematic center. This peak fractional abundance at the outer CMZ is comparable to that in the Milky Way CMZ, and orders of magnitude higher than that in Galactic disk, star-forming regions. From the range of $HOCO^+/CO_2$ ratios suggested from chemical models, the gas-phase CO_2 fractional abundance is estimated to be (1–20) $\times 10^{-7}$ at the outer CMZ, and orders of magnitude lower near the center. We estimate the CO_2 ice fractional abundances at the outer CMZ to be (2–5) $\times 10^{-6}$ from the literature. A comparison between the ice and gas CO_2 abundances suggests an efficient sublimation mechanism. This sublimation is attributed to large-scale shocks at the orbital intersections of the bar and CMZ.

Unified Astronomy Thesaurus concepts: Astrochemistry (75); Interstellar medium (847); Starburst galaxies (1570); Interstellar molecules (849); Molecular clouds (1072)

1. Introduction

The abundance of interstellar molecules depends on the balance between their formation and destruction processes in the gas phase and on grain surfaces. Exchange processes can transform molecules in one phase to another; gas-phase molecules can freeze onto dust grains as ice (adsorption), while molecules on grain surfaces can sublimate into the gas phase (desorption). Knowing both the gas- and ice-phase abundances is, therefore, necessary for a comprehensive understanding of their chemical composition and their related physical conditions. Carbon dioxide (CO_2) is one of the most dominant forms of ice on interstellar dust (Öberg et al. 2011) together with H_2O and CO. CO_2 is, in fact, one of the ice species detectable in extragalactic sources (e.g., Lahuis et al. 2007; Yamagishi et al. 2015). It is obvious from strong CO rotational emission that the gas-phase CO is abundant, but CO_2 is thought to reside more preferentially on dust due to inefficient gas-phase formation (Garrod & Pauly 2011). Because CO_2 has a higher desorption energy than that of CO, the presence of abundant gas-phase CO_2 requires stronger desorption mechanisms. While CO_2 can be detected via rotational–vibrational transitions in warm gas ($\gtrsim$several 100 K) (e.g., Boonman et al. 2003) or in ice with broader line features (e.g., Yamagishi et al. 2015), it cannot be observed in cold gas due to the lack of a permanent dipole moment.

Although the gas-phase abundances of such species without a dipole moment cannot be directly measured through

[18] Jansky Fellow of the National Radio Astronomy Observatory.

commonly observed rotational transitions, it has been proposed that they can be estimated from their protonated forms (Herbst et al. 1977; Agúndez et al. 2015; Rivilla et al. 2019). The protonated form of CO_2, $HOCO^+$, was first detected in Sgr B2 by Thaddeus et al. (1981), but its line identification required spectroscopic confirmation by Defrees et al. (1982). Since then, $HOCO^+$ has been detected in translucent clouds (Turner et al. 1999), low-/high-mass star-forming regions (Sakai et al. 2008; Vastel et al. 2016; Fontani et al. 2018; Majumdar et al. 2018), the Galactic Center (Sgr A and B2 clouds; Minh et al. 1988, 1991), starburst galaxies (Martín et al. 2006; Aladro et al. 2015) and a $z \sim 0.9$ molecular absorber (Muller et al. 2013). Among them, Minh et al. (1991) and Armijos-Abendaño et al. (2015) found about two orders of magnitude higher fractional abundances of $HOCO^+$ in the Galactic Center than in spiral-arm molecular clouds.

The main formation paths of $HOCO^+$ are gas-phase reactions, including the protonation of CO_2 such as (Vastel et al. 2016; Bizzocchi et al. 2017)

$$CO_2 + H_3^+ \longrightarrow HOCO^+ + H_2,$$

or an ion-neutral reaction

$$HCO^+ + OH \longrightarrow HOCO^+ + H.$$

In the former route, the $HOCO^+$ abundance can increase due to the evaporation of CO_2 from grain surfaces because CO_2 is one of the most abundant forms of carbon on grain surfaces. Ice can sublimate thermally (e.g., in the vicinity of protostars), or nonthermally (e.g., photodesorption, cosmic-ray-induced evaporation, or shock sputtering). While the latter route from HCO^+ is considered dominant in at least some parts of high- or low-mass star-forming regions (Fontani et al. 2018; Majumdar et al. 2018), the protonation of CO_2 can be the dominant route when there is a fast mechanism of CO_2 sublimation.

Shocks, one such driver of the ice sublimation process, are ubiquitous in galactic centers. In many barred-spiral galaxies, galactic centers host intersections of x_1 and x_2 orbits[19] (Athanassoula 1992; Seo & Kim 2013; Sormani & Li 2020). At these orbital intersections, shocks are naturally expected. The abundances of typical shock molecular tracers such as CH_3OH and SiO have been found to be enhanced at locations of orbital intersections in IC342 and M83 (Meier & Turner 2005; Harada et al. 2019).

In this paper, we report an enhancement of $HOCO^+$ at the orbital intersections near the center of the starburst galaxy NGC 253. NGC 253 is one of the nearest ($d = 3.5$ Mpc; Rekola et al. 2005) and most studied starburst galaxies. Its nuclear ring forms a central molecular zone (CMZ) within a few hundred parsec scale, with a mass of $\sim 2 \times 10^8\,M_\odot$ within a radius of $r = 150$ pc (Leroy et al. 2015). This large reservoir of molecular gas enables active star formation (Sakamoto et al. 2006, 2011; Bolatto et al. 2013; Krieger et al. 2019; Rico-Villas et al. 2020), which affects the properties of the molecular gas (e.g., through heating; Mangum et al. 2019). Gas in the bar orbit (x_1 orbits) is being fed to the center of NGC 253 (x_2 orbits), and shocks are expected when this gas flow collides with the nuclear ring, as discussed above for other galaxies. Figure 1 (left) shows IRAC 8 μm (Dale et al. 2009; LVL team 2009) and CO(2-1) integrated-intensity (Atacama Large Millimeter/submillimeter Array, ALMA, data 2018.1.01321.S; PI: Faesi) images covering most of NGC 253 to indicate the locations of these orbits. The association between shocks at orbital intersections and chemistry has been proposed by García-Burillo et al. (2000) and Meier et al. (2015).

At the center of NGC 253, a large number of molecular species are detectable (Martín et al. 2006; Meier et al. 2015). To fully explore the chemical complexity in this galaxy, we conducted the ALMA large program ALMA Comprehensive High-resolution Extragalactic Molecular Inventory (ALCHEMI; Martín et al. 2021). ALCHEMI is a wide-frequency, unbiased spectral scan mosaic toward the CMZ of NGC 253 at a common 1.″6 resolution. This survey has discovered high cosmic-ray ionization rates (Holdship et al. 2021; Harada et al. 2021; Holdship et al. 2022), detected a phosphorus-bearing species for the first time in an extragalactic source (Haasler et al. 2022), and detected methanol masers (Humire et al. 2022) in the CMZ of NGC 253. We utilize the ALCHEMI data to study the multiple transitions of $HOCO^+$.

This paper is organized as follows. Section 2 describes our observational parameters and data analysis, and images of the integrated intensities are presented in Section 3. The derived column densities of $HOCO^+$ are shown in Section 4, while the $HOCO^+/CO_2$ ratios are discussed using chemical models in Section 5. In Section 6, we discuss our results including a comparison with ice abundances. Our results are summarized in Section 7.

2. Observations and Data Analysis

The ALCHEMI spectral survey mosaic of the NGC 253 CMZ was performed between 2017 and 2019, with ALMA's 12 m antenna and 7 m antenna arrays. It covered a broad frequency range between 84 and 373 GHz (Bands 3 to 7, avoiding deep atmospheric lines), down to sensitivities of $\sim$10 mK per 10 km s^{-1} channel. The ALCHEMI data products have a uniform angular resolution of 1.″6 and cover a field of view of 50″ × 20″ centered on the CMZ of NGC 253 (phase center: $\alpha = 00^h47^m33\overset{s}{.}28$, $\delta = -25°17'17\overset{''}{.}7$, in the International Celestial Reference System, ICRS). The extent of the largest recoverable angular scale is greater than or equal to 15″. A detailed description of the ALCHEMI survey products can be found in Martín et al. (2021).

We extracted the line cubes around the transitions of $HOCO^+$ with a velocity resolution binned to 10 km s^{-1}. Within the $\sim$290 GHz coverage of the ALCHEMI survey, we find 14 detectable $HOCO^+$ transitions, occurring every $\sim$21.4 GHz. However, some transitions are severely blended with transitions from other species and are not used in this analysis. The spectroscopic parameters and spectral channel rms values for the $HOCO^+$ transitions used in this paper are listed in Table 1.

3. Integrated Intensities

Figures 2(a)–(d) show the velocity-integrated-intensity (moment 0) images of $HOCO^+$ in multiple transitions (see Table 1 for their properties). Many transitions used in this work have neighboring lines, and it is not possible to make the moment 0 images simply by collapsing neighboring channels. To exclude this contamination, we applied a 3D mask made from position–position–velocity space by only including pixels

[19] Bars lie on x_1 orbits, while x_2 orbits form inner nuclear rings. The location of nuclear rings may correspond to that of inner Lindblad resonances, but this is not always the case (Kim et al. 2012).

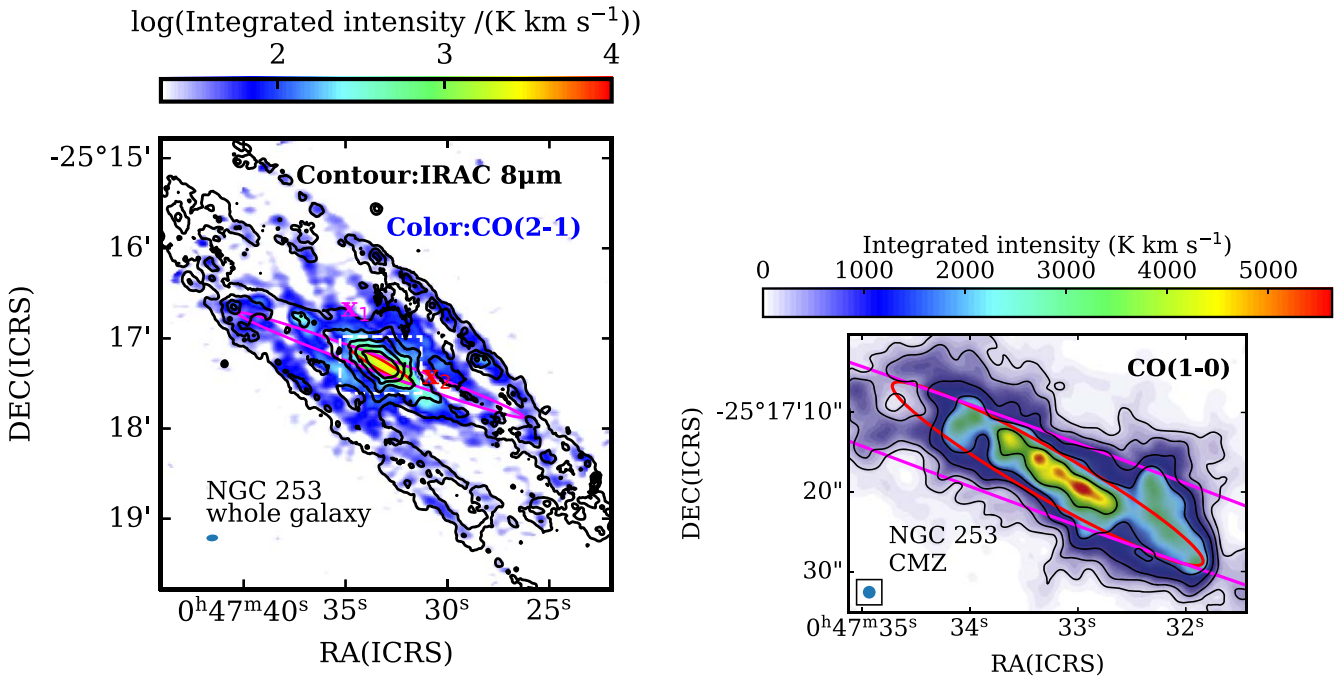

Figure 1. Left: the IRAC 8 μm image is shown with contours, while the integrated-intensity image of CO(2-1) is shown with color in the logarithmic scale. The contour levels are 25, 50, 100, 200, and 500 MJy msr^{-1}. The approximate positions of the bar orbits (x_1 orbits) and inner orbits that form the CMZ (x_2 orbits) are shown with magenta and red ellipses, respectively. The beam size is shown as a blue ellipse in the left-bottom corner. The area shown in Figure 2 and the right panel are indicated with a white dashed rectangle in Figure 2 (left). For more detailed orbit models, we refer the reader to other works (e.g., Sorai et al. 2000; Das et al. 2001; Levy et al. 2022). Right: the integrated-intensity image of CO(1-0) overlaid with the same orbits as the left panel.

Table 1
$HOCO^+$ Spectroscopic Properties and rms Noise Values

Transition	$\nu^{(a)}_{\rm rest}$ (GHz)	$E^{(b)}_{\rm up}$ (K)	$\log(A_{\rm ul})^{(c)}$ (s^{-1})	rms $^{(d)}$ (mJy beam^{-1})	rms $^{(e)}$ (mK)	Blending $^{(f)}$
$4_{0,4}$-$3_{0,3}$	85.531	10.3	−4.63	0.19	12.	Potential blending with CH_3CCH. Minor blending with U-lines
$5_{0,5}$-$4_{0,4}$	106.914	15.4	−4.33	0.20	8.4	N/A
$6_{0,6}$-$5_{0,5}$	128.295	21.6	−4.08	0.33	9.5	Minor blending with U-lines
$7_{0,7}$-$6_{0,6}$	149.676	28.7	−3.88	0.42	9.0	Potential blending with U-lines
$8_{0,8}$-$7_{0,7}$	171.056	36.9	−3.70	0.75	12.	Potential blending with CH_3CCH.
$12_{0,12}$-$11_{0,11}$	256.566	80.0	−3.16	0.99	7.2	Potential blending with CH_3CCH, HC_3N $v7=2$
Transitions below were not used for analysis						
$9_{0,9}$-$8_{0,8}$	192.435	46.2	−3.54			Blended with U-line
$10_{0,10}$-$9_{0,9}$	213.813	56.4	−3.40			Blended with C_2H_5OH
$11_{0,11}$-$10_{0,10}$	235.190	67.7	−3.28			Blended with SO_2
$13_{0,13}$-$12_{0,12}$	277.941	93.4	−3.06			Blended with U-line
$14_{0,14}$-$13_{0,13}$	299.314	107.7	−2.96			Non detection
$15_{0,15}$-$14_{0,14}$	320.686	123.1	−2.87			Non detection
$16_{0,16}$-$15_{0,15}$	342.056	139.6	−2.78			Non detection
$17_{0,17}$-$16_{0,16}$	363.424	157.0	−2.70			Non detection

Note. (*a*) Rest frequency. (*b*) Upper level energy of the transition. (*c*) A_{ul}: Einstein coefficient of spontaneous emission. All values were taken from the Cologne Database for Molecular Spectroscopy (CDMS; https://cdms.astro.uni-koeln.de; Müller et al. 2001, 2005; Bizzocchi et al. 2017). (d) and (e) rms values of a single channel with $\Delta v = 10$ km s^{-1} in mJy beam^{-1} and mK units. (f) Presence of blending; transitions are shown with quantum numbers J_{K_a,K_c}. Only $K_a = 0$ transitions are shown because transitions with $K_a \neq 0$ are not detected due to their higher energy state and lower Einstein coefficients. The upper part of this table shows transitions used for the analyses of this paper, whose line shapes are separable from neighboring lines. The lower part lists transitions with severe blending or without reliable detections. "Potential blending" means the case where the line centers are separated by more than 200 km s^{-1}, but the line wings can contaminate the moment maps of the $HOCO^+$ transitions.

with CO $J = 1 - 0$ detections above the 20σ level. The 20σ cutoff may sound unnecessarily high, but the signal-to-noise ratios of $HOCO^+$ transitions are more than 100 times lower than that of CO(1-0). Therefore, this mask does not exclude any notable $HOCO^+$ emission, but helps to exclude contamination from nitrogen sulfide transitions neighboring with CO(1-0) to be included in the integrated-intensity map. Despite the elimination of contamination with this mask, the only transition that is free from contamination is $5_{0,5}-4_{0,4}$ (Figure 2(a)). Other images that are relatively less affected by

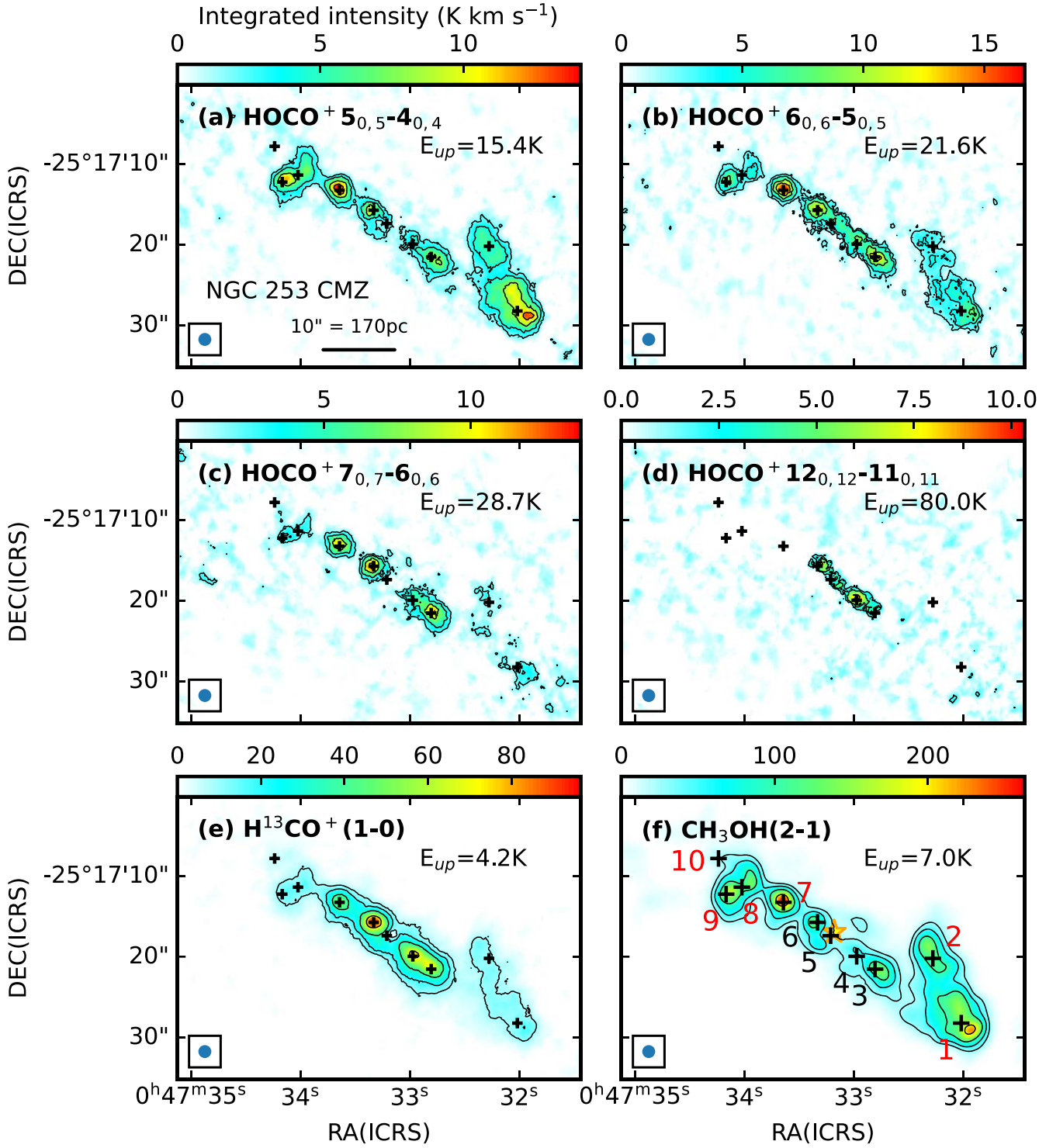

Figure 2. Velocity-integrated-intensity maps of (a–d) four $HOCO^+$ transitions, (e) $H^{13}CO^+$(1-0), and (f) $CH_3OH(2_k-1_k)$. Contour levels are (a–d) [2, 4, 8, 12], (e) [9.0, 18.0, 36.0, 72.0], and (f) [25.0, 50.0, 100.0, 200.0] K km s^{-1}. A beam size of $1\farcs6 \times 1\farcs6$ (27 pc × 27 pc) is shown at the bottom left corner in each panel as a blue circle. Locations of the GMCs identified by Leroy et al. (2015) are shown as black crosses and labeled in panel (f). The coordinates of these GMCs are given in Table 3. The kinematic center known as "TH2" (Turner & Ho 1985) with the revised coordinates of Cohen et al. (2020) is shown as a yellow star with orange edges in panel (f). GMCs with Class I methanol maser detection by Humire et al. (2022) are labeled with red numbers in panel (f).

blending are also shown in Figure 2 (panels b–d). The level of contamination is usually very low (<10%) except for giant molecular cloud (GMC) 5, where there is little $HOCO^+$ emission and stronger emission from neighboring lines. Transitions $4_{0,4}-3_{0,3}$ and $8_{0,8}-7_{0,7}$ can still be used to obtain column densities as we use spectral fitting, but their images are not shown. A low-excitation line of $HOCO^+$ ($5_{0,5}-4_{0,4}$; $E_{up} = 15.4$ K) shows peaks near the outer CMZ, in GMCs 1, 7, and 9 (GMC numbering is shown in panel (f); Leroy et al. 2015; see also Appendix C for coordinates). On the other hand, the higher-excitation transitions ($E_{up} \gtrsim 30$ K) peak closer to the center (GMCs 3 and 6).

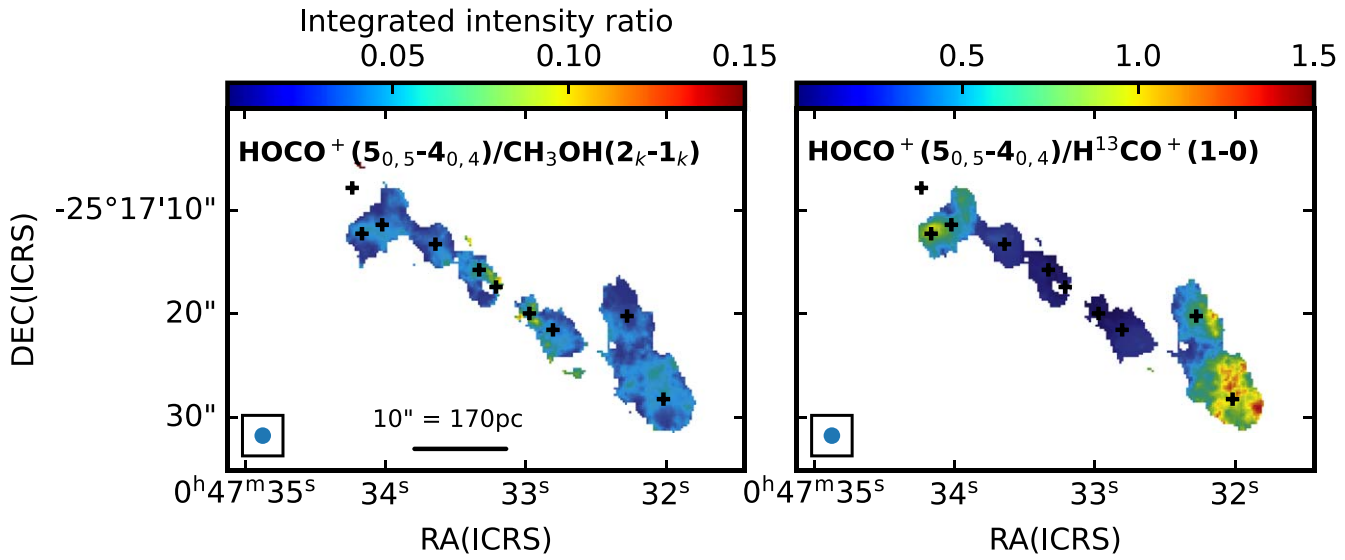

Figure 3. Integrated intensity ratios of (left) $HOCO^+(5_{0,5}-4_{0,4})/CH_3OH$ (2_k-1_k) and (right) $HOCO^+(5_{0,5}-4_{0,4})/H^{13}CO^+$(1-0). Only pixels with an integrated intensity of $>3\sigma$ for each transition and ratio are shown. The ranges of the color scales are set to 0.003–0.15 (left) and 0.03–1.5 (right). Because the maximum/minimum ratios of the color scales are 50 for both images, the variations in color scales between the left and right panels represent variations in the $HOCO^+(5_{0,5}-4_{0,4})/CH_3OH$ (2_k-1_k) and $HOCO^+(5_{0,5}-4_{0,4})/H^{13}CO^+$(1-0) ratios.

Panels (e) and (f) of Figure 2 show integrated-intensity images of $CH_3OH(2_k-1_k)$ (group of transitions at $\nu_{rest}\sim96.74$ GHz with the strongest transition $2_0^+-1_0^+$)[20] and $H^{13}CO^+$(1-0) ($\nu_{rest}=86.75$ GHz) for comparison. The emission distribution of $CH_3OH(2_k-1_k)$ is similar to that of the low-J transitions of $HOCO^+$, as well as the low-J transitions of HNCO, and SiO (Meier et al. 2015; K.-Y. Huang et al., 2022, in preparation). On the other hand, the distribution of $H^{13}CO^+$(1-0), which is rather similar to that of molecules with strong emission (e.g., CO, HCO^+, HCN, CS, etc.; Meier et al. 2015; Martín et al. 2021), is clearly different from that of $HOCO^+$. The $H^{13}CO^+$(1-0) emission is concentrated near the center of NGC 253 (GMCs 3–7) instead of the outer CMZ.

The similarity between the integrated intensities of $HOCO^+$ $(5_{0,5}-4_{0,4})$ and CH_3OH (2_k-1_k) and the difference between those of $HOCO^+$ $(5_{0,5}-4_{0,4})$ and $H^{13}CO^+$(1-0) are highlighted in Figure 3. While the $HOCO^+(5_{0,5}-4_{0,4})/CH_3OH$ (2_k-1_k) ratios are relatively constant, the $HOCO^+(5_{0,5}-4_{0,4})/H^{13}CO^+$(1-0) ratio varies significantly. All these transitions have relatively low upper state energies ($HOCO^+$ $(5_{0,5}-4_{0,4})$: $E_u=15.4$ K; CH_3OH $(2_0^+-1_0^+)$: $E_u=7.0$ K; $H^{13}CO^+$(1-0): $E_u=4.2$ K), and these ratio maps should be good proxies for the variations in column densities of these molecules.

4. Column Densities and Fractional Abundances

Figure 4(a) shows a column-density map of $HOCO^+$. These column densities were derived using the public software CASSIS[21] (Vastel et al. 2015) supplied with spectroscopic constants from the spectroscopic database from the CDMS (Müller et al. 2001, 2005). CASSIS calculates molecular column densities based on input spectral line brightness temperatures with consideration of optical depths, either with an LTE assumption or, if collisional rates are available, non-LTE assumption. We used a Markov Chain Monte Carlo (MCMC) algorithm assuming LTE to fit the column densities, excitation temperatures, line velocities, and line widths (see Appendix A). The column densities were calculated only for pixels with a $>3\sigma$ detection of both $HOCO^+(4_{0,4}-3_{0,3})$ and $HOCO^+(5_{0,5}-4_{0,4})$ at velocities within 30 km s^{-1} from the line center. Line-center velocities used for this 3σ detection criterion are determined from the image cube of CO(1-0) from the ALCHEMI data. These line-center velocities from CO may be different from the $HOCO^+$ velocities fitted from CASSIS. Instead of deriving the column densities and excitation temperatures on a pixel-by-pixel basis, we bin the intensities within hexagonal pixels with a horizontal length of 0.″8, half of the image spatial resolution of 1.″6, to reduce the computational time running CASSIS. Examples of the spectral fitting are shown for hexagonal pixels located at $(x_{offset}, y_{offset})=(-17.''3, -10.''4)$ and $(2.''0, 2.''1)$ in Figure 5, where the offset is taken from the phase center. In general, the observed spectra fit well with the LTE spectra. The resulting column-density distribution appears similar to that of the moment 0 images of low-excitation transitions (e.g., Figure 2(a)).

The excitation temperatures derived from the above spectral fitting are shown in Figure 4(b). While regions far from the kinematic center[22] of NGC 253 show low excitation temperatures of $\lesssim$10 K (GMCs 1, 2, 8, and 9), the excitation temperatures become higher, up to 40 K, near the center of NGC 253 (GMCs 3 and 6).

We also obtain the total hydrogen column densities (Figure 4(c)) to calculate the fractional abundances of $HOCO^+$ (i.e., the $HOCO^+$ column density divided by the total hydrogen column density $N(H_2)$). The total H_2 column densities were derived from the dust continuum image at 361.5 GHz shown by Harada et al. (2021) with the derivation method based on Hildebrand (1983) for pixels above 3σ

[20] These transitions may not be in local thermodynamic equilibrium (LTE), but are "quasi-thermal" and they are not identified as masing (Humire et al. 2022).
[21] http://cassis.irap.omp.eu/

[22] The kinematic center of NGC 253 is located near GMC 5 (Turner & Ho 1985; Müller-Sánchez et al. 2010). Although there is a debate on the exact location of the kinematic center, the difference of 0.″7 appearing in the literature does not affect our discussion.

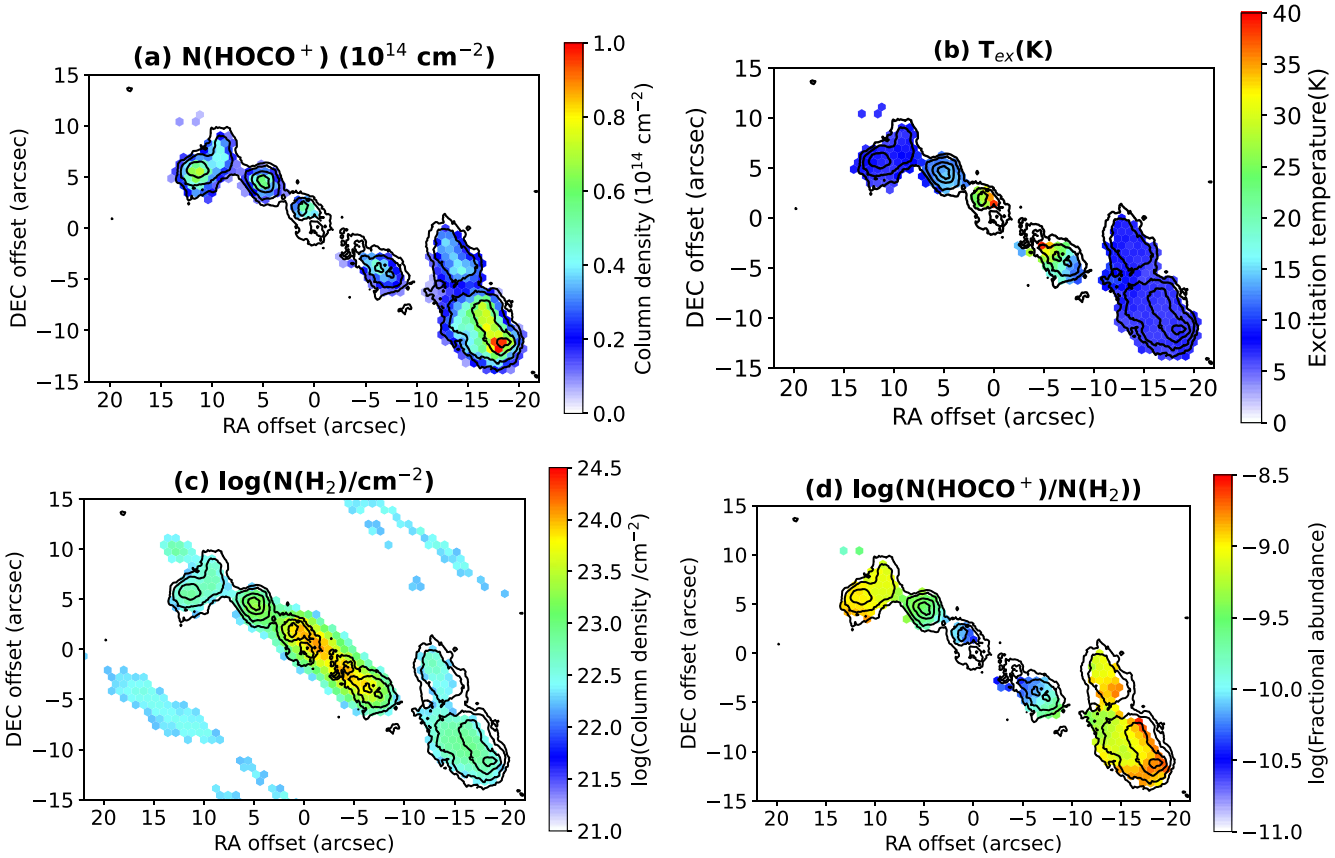

Figure 4. Maps of (a) the $HOCO^+$ column density, (b) the excitation temperature of $HOCO^+$derived from CASSIS, (c) the total H_2 column density derived from the dust continuum shown in a logarithmic scale, and (d) the fractional abundance of $HOCO^+$ shown in the logarithmic scale. The black contours show the $HOCO^+$ ($5_{0,5}$–$4_{0,4}$) integrated intensities, as in Figure 2.

detection. A simplified formula is given as Equation (3) in Mangum et al. (2019)

$$N(H_2)(\mathrm{cm}^{-2}) \sim 7.0 \times 10^{22} R_{dg} \left(\frac{\lambda(\mathrm{mm})}{0.4}\right)^{\beta} \frac{T_R(\mathrm{K})}{T_d(\mathrm{K})}, \quad (1)$$

where $N(H_2)$ is the molecular hydrogen column density, R_{dg} is the dust-to-gas mass ratio, λ is the wavelength, T_R is the radiation temperature, and T_d is the dust temperature. This formula is valid for $h\nu \ll kT_d$ (the Rayleigh–Jeans approximation). We use an emissivity of $\beta = 1.5$, a dust temperature of $T_{\mathrm{dust}} = 30$ K, and a dust-to-gas mass ratio of 150 following Mangum et al. (2019). This estimate of the dust temperature is close to the observed value, but some dust components may be warmer. Pérez-Beaupuits et al. (2018) derived dust temperature components of 37, 70, and 188 K in the central region of NGC 253 using their assumed source size of $17\farcs3 \times 9\farcs2$ from their Herschel and SOFIA observations. These components contain mass fractions of 65, 26, and 9%, respectively. If the dust is warmer, the actual column density should be smaller by a similar factor; for instance, a factor of 5 smaller if $T_{\mathrm{dust}} = 150$ K. The column-density dependence on the dust temperature becomes larger than $\propto \frac{1}{T_d}$ when the dust is cold ($T_d \lesssim 20$ K) and one cannot use the Rayleigh–Jeans approximation, but we expect that there is a very small amount of cold dust in the center of NGC 253.

The fractional abundance of $HOCO^+$ is higher at larger distances from the center of NGC 253, and it decreases by more than an order of magnitude at the center (Figure 4(d)). At the peaks of $HOCO^+$(GMCs 1, 8, and 9), the fractional abundance is $\sim$(1–2) $\times 10^{-9}$, similar to those observed in Galactic center clouds: (2–8) $\times 10^{-9}$ (Minh et al. 1991; Armijos-Abendaño et al. 2015). On the other hand, it is orders of magnitude higher than those observed in Galactic disk clouds, which range from 10^{-13} to 5×10^{-11} (Vastel et al. 2016; Fontani et al. 2018; Majumdar et al. 2018).

5. $HOCO^+/CO_2$ Ratios

To estimate the gas-phase abundances of CO_2 from $HOCO^+$, we ran chemical abundance models based on Nautilus (Ruaud et al. 2016), accounting for gas, ice surface, and ice mantle phases. In addition to the thermal evaporation, desorption from dust heating due to cosmic rays (Hasegawa & Herbst 1993) is included in the model. Desorption through the cosmic-ray heating of dust is where the dust grain is temporarily heated to a certain maximum temperature for a very short timescale ($\sim 10^{-5}$ s), which then cools down. The model also includes photodesorption (Öberg et al. 2009a, 2009b) both from direct UV photons and cosmic-ray-induced UV photons with a default yield of 10^{-4} for all the grain species. We also ran a model with a desorption yield of 10^{-3} for CO_2. Our models do not include shocks. We calculated grid models with varying densities ($n = 10^3$–10^6 cm^{-3}) and cosmic-ray ionization rates ($\zeta = 10^{-17}$–10^{-12} s^{-1}) following a similar approach as Harada et al. (2021). Temperatures were calculated with the Meudon photodissociation region (PDR) code (ver. 1.5.4) (Le Petit et al. 2006) (Figure 6(a)), and were fed to Nautilus to run chemical

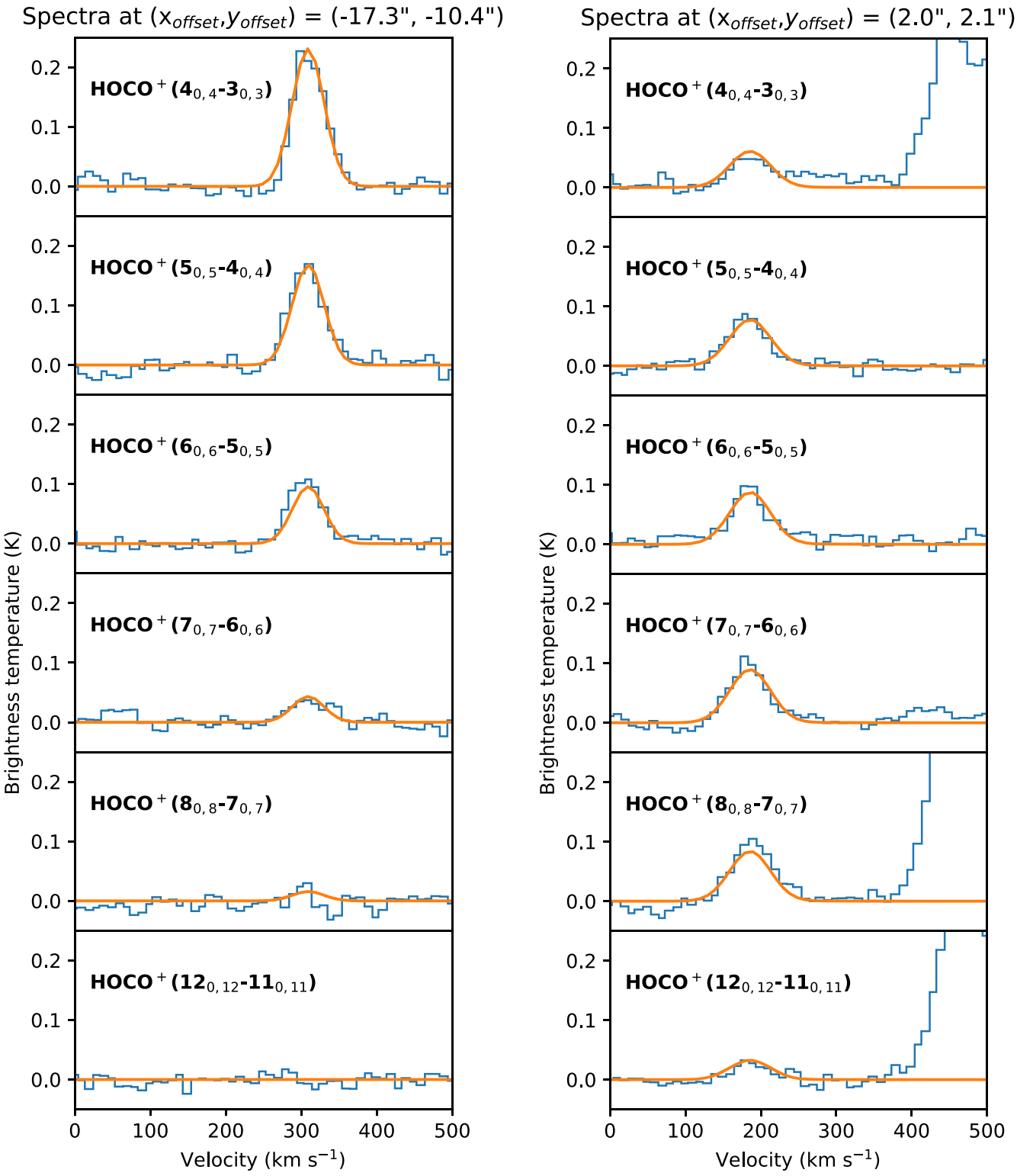

Figure 5. Examples of observed spectra (blue) vs. modeled spectra from CASSIS (orange) at ($x_{\rm offset}$, $y_{\rm offset}$) of (Left) (-17.″3,-10.″4) and (Right) (2.″0,2.″1) relative to the phase center of our observations.

abundance models with a larger chemical network. Despite the high gas temperature with the high cosmic-ray ionization rate ($T > 1000$ K when $\zeta = 10^{-12}$ s^{-1} and $n = 10^3$ cm^{-1}), the dust temperature calculated from the Meudon code remains cold, around 11 K. We adopted a maximum visual extinction of $A_{\rm V} = 20$ mag with a turbulent velocity of 1 km s^{-1}, and used the temperature in the model at $A_{\rm V} = 10$ mag (Figure 6(d)), where the effects of the PDRs are negligible. We note that, unlike in the description of the observational results, the fractional abundances are expressed as abundances of certain species over the total hydrogen abundance ($N_{\rm Htotal} = N_{\rm Hatom} + 2N_{\rm H2}$), instead of as molecular hydrogen abundances.

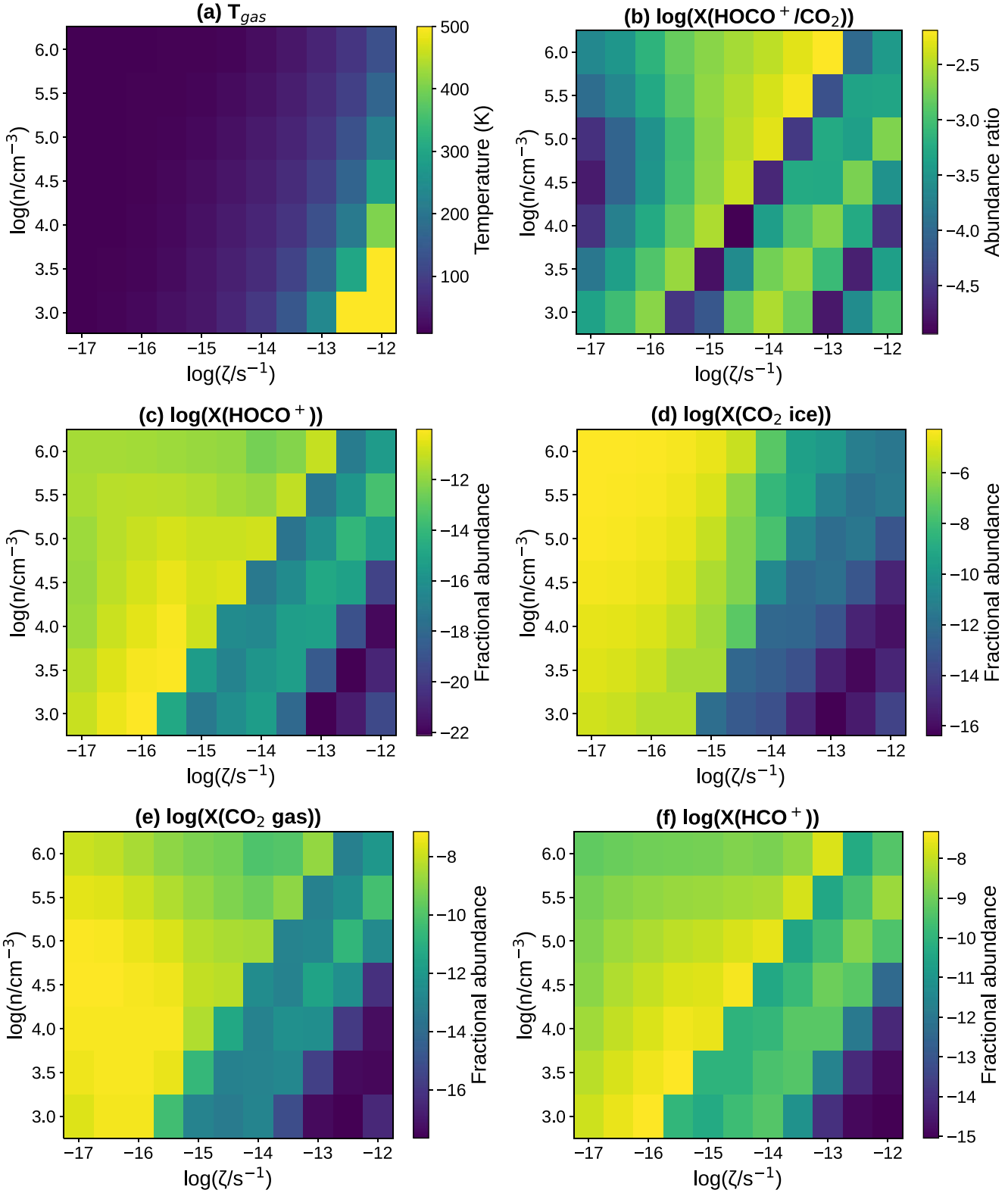

Figure 6. The following modeled quantities are shown as functions of the density and cosmic-ray ionization rate: (a) gas temperatures from the Meudon code used for Nautilus chemical modeling, (b) abundance ratios $HOCO^+/CO_2$, (c) fractional abundances of $HOCO^+$, (d) CO_2 ice (surface + mantle), and (e) CO_2 gas, and (f) HCO+.

Figure 6(b) shows the $HOCO^+/CO_2$ abundance ratios in the gas phase, that vary between 10^{-5} and 10^{-2} for the most part. Previous ALCHEMI studies have suggested that the cosmic-ray ionization rates in NGC 253 are at least a few orders of magnitude higher than that in Galactic spiral-arm clouds (Holdship et al. 2021; Harada et al. 2021; Holdship et al. 2022), which increases the $HOCO^+/CO_2$ abundance ratios due to an increased H_3^+ abundance. Although the cosmic-ray ionization rates are expected to be high, extremely high rates ($\zeta \gtrsim 10^{-13}$ s^{-1} for $n = 10^5$ cm^{-3}) would destroy $HOCO^+$ (Figure 6(c)),

especially in lower-density regions. Therefore, we consider $HOCO^+/CO_2$ ratios of $\sim 10^{-3}$–10^{-2} in the latter sections, which are taken from the parameter space where the $HOCO^+$ abundance is moderately high.[23]

It is worth noting that cosmic-ray-induced desorption mechanisms do not change the abundances significantly. This is because cosmic-ray-induced photodissociation is a more efficient form of destruction than desorption if the desorption yield is on the order of 10^{-3} or lower. According to Öberg et al. (2009b), the photodesorption yield of CO_2 cannot go higher than a few times 10^{-3}, which means photodesorption is not significant. The desorption of CO_2 due to cosmic-ray heating of dust has an even lower effect than the photodesorption for models run with the commonly used maximum dust temperature of 70 K.

In our model, the dominant formation reactions of $HOCO^+$ vary with time. In general, the protonation of CO_2 is more dominant at early times ($<10^5$ yr), and the gas-phase production with HCO^+ and OH becomes more efficient in later times (see Section 1). However, the dominant formation routes also vary with physical conditions and it is difficult to conclude which one is more dominant.

Although our models do not include shocks, but we argue that this approach should be sufficient to estimate the $HOCO^+/CO_2$ ratios, especially their upper limits. The $HOCO^+/CO_2$ ratios are determined by the balance among the protonation of CO_2, electron recombination of $HOCO^+$, proton transfer from $HOCO^+$ to species with a higher proton affinity than CO_2, and the ion-neutral production of $HOCO^+(HCO^+ + OH)$. These reactions occur regardless of shocks. If shocks evaporate CO_2 significantly, there should be less contribution to $HOCO^+$ formation through HCO^+ and OH compared with the protonation of CO_2, and the $HOCO^+/CO_2$ ratios should be lower, while shocks should increase the fractional abundances of both $HOCO^+$ and CO_2. Therefore, our models without shocks are likely sufficient to obtain upper limits of the $HOCO^+/CO_2$ ratios, but more realistic modeling with shocks will be conducted as future work. It should also be noted that the models without shocks severely underproduce the $HOCO^+$ fractional abundances compared with the observed peak values, which implies the need for shocks to explain the observed abundances (see Section 6.1). We include the gas-neutral reaction of $HCO^+ + OH$ and many other related reactions in the model. The fact that our model could not reproduce the observed fractional abundances suggests that the formation route through this reaction is not enough to explain our observations.

6. Discussion

6.1. Origins of the $HOCO^+$ Emission

As discussed earlier, the formation routes of $HOCO^+$ do not have to involve the protonation of CO_2. The gas-phase reaction between HCO^+ and OH may also contribute to $HOCO^+$. Fontani et al. (2018) argued that $HOCO^+$ must be formed via the reaction above ($HCO^+ + OH$; see Section 1) in high-mass star-forming cores because the $HOCO^+$ fractional abundances derived from the $4_{0,4}$–$3_{0,3}$ transition are correlated with the fractional abundances of $H^{13}CO^+$, while there is no correlation with that of methanol. If $HOCO^+$ is formed via protonation, a large amount of evaporated CO_2 must be present, which also implies a large amount of methanol in the gas phase. This is because methanol is formed on the ice, and its gas-phase production is extremely inefficient (Garrod et al. 2007).

The CMZ of NGC 253 shows a different trend from the case of these high-mass star-forming cores. We do see a positive spatial correlation between $HOCO^+$ and CH_3OH with low-excitation transitions of both molecules enhanced at the outer CMZ of NGC 253 (Figure 3). Meanwhile, the correlation between $HOCO^+$ and $H^{13}CO^+$ is weak because $H^{13}CO^+$ is more abundant near the center of the CMZ (Figure 3; see also Harada et al. 2021, for the abundances of $H^{13}CO^+$). There is a caveat that the ice composition may be different in the high-mass star-forming regions observed by Fontani et al. (2018) and the NGC 253 CMZ, and the presence or lack of correlation may not necessarily imply a difference in formation routes. On the other hand, the presence of a correlation between CH_3OH and $HOCO^+$ and the lack of correlation between $HOCO^+$ and most other species (e.g., CO, HCN, HCO^+, etc.) strongly suggest a similar mechanism enhancing the abundances of both CH_3OH and $HOCO^+$. This mechanism must involve desorption, as methanol is only efficiently formed on ice. Therefore, we argue that $HOCO^+$ in our observations is likely formed from CO_2 through protonation.

6.2. Inferred Gas-phase CO_2 Fractional Abundances

If $HOCO^+$ is produced through the protonation of CO_2, as we discussed above, CO_2 must be evaporated from ice into the gas phase because CO_2 is much more abundant in ice than in the gas phase (Figure 6(d)). Obtaining the gas-phase fractional abundances of CO_2 could provide essential hints helping us to evaluate the origin of the gas-phase CO_2. From the chemical model, we find that the range of the $HOCO^+/CO_2$ ratio is $\sim$0.001–0.01. Because the maximum fractional abundance of $HOCO^+$ is $\sim 2 \times 10^{-9}$ in GMC 1 and $\sim 1 \times 10^{-9}$ in GMCs 2, 8, and 9, the gas-phase CO_2 fractional abundances can be $(1\text{–}20) \times 10^{-7}$ at the outer CMZ, where the $HOCO^+$ intensity peaks.

6.3. Comparison with Ice Observations of CO_2

Here we compare the fractional abundance of CO_2 gas estimated above with that of the CO_2 ice observations. We utilize the CO_2 column densities of selected regions of AKARI observations made by Yamagishi et al. (2015). Although this reference describes these observations in detail, we have included a summary of them in Appendix B. These observations were made with a rectangle slit with a size of $5'' \times 5.''8$ (Figure 7, left). Subsequently, we extracted the values of the continuum flux from the same regions to estimate the total H_2 column density using the method described in Section 4. We then derived the fractional abundances of CO_2 in the ice phase in these regions, as shown in Figure 7 (right). We note that the components traced by CO_2 ice likely come from relatively lower-column-density regions than the ones traced by the dust continuum. Therefore, we have to be aware of the caveat that our estimations of the CO_2 fractional abundances are rather crude, only accurate for an order-of-magnitude approximation.

[23] We note that the presence of $HOCO^+$ is still consistent with the cosmic-ray ionization rates derived by Holdship et al. (2021) and Harada et al. (2021) ($\zeta \gtrsim 10^{-14}$ s^{-1} for $n = 10^5$ cm^{-3}), but the value obtained by Holdship et al. (2022) ($\zeta \sim 10^{-13}$ s^{-1} for $n = 10^5$ cm^{-3}) would not allow high fractional abundances of $HOCO^+$.

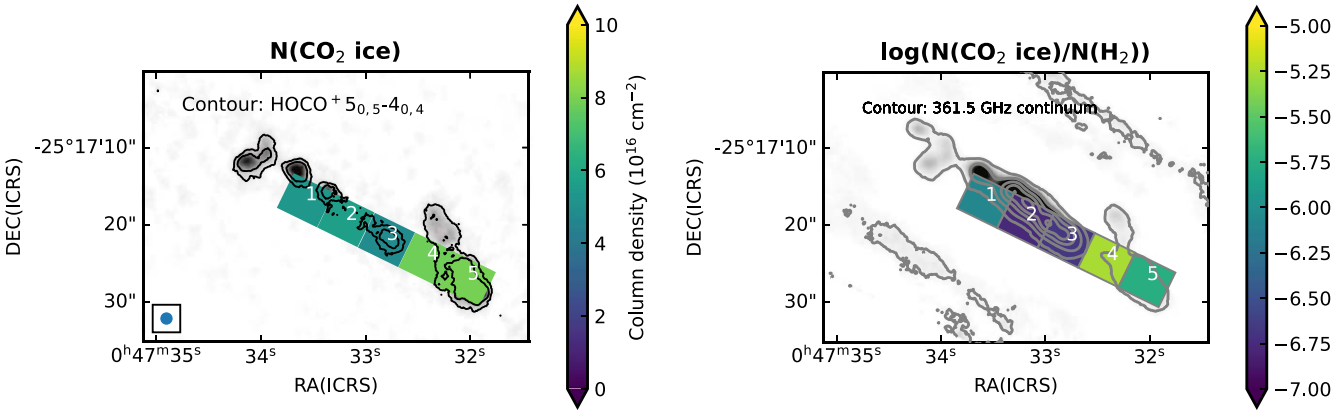

Figure 7. Left: the column densities of CO_2 ice reported by Yamagishi et al. (2015) are shown for selected slits in color. The integrated-intensity image of $HOCO^+$ ($5_{0,5}$–$4_{0,4}$) is shown both in contours and gray scale. Right: the fractional abundances of CO_2 ice (i.e., CO_2 ice column density divided by the averaged total H_2 column density inside the rectangular regions) are shown in log scale with colored rectangles. The continuum image at 361.5 GHz is shown in contours and gray scale.

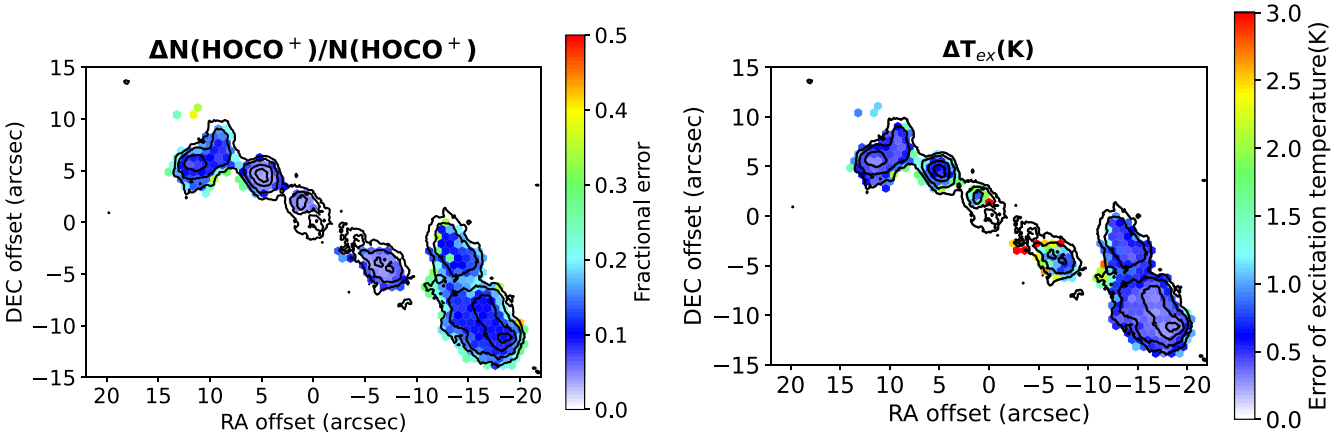

Figure 8. Left: ratios of errors in the derivation of $HOCO^+$ column densities over the derived $HOCO^+$ column densities at corresponding hexagonal pixels. Right: errors of the excitation temperatures.

Table 2
Modeled Integrated Intensities

GMC	x_{offset} (″)	y_{offset} (″)	$\int Idv$ (K km s^{-1})					
			$(4_{0,4}-3_{0,3})$	$(5_{0,5}-4_{0,4})$	$(6_{0,6}-5_{0,5})$	$(7_{0,7}-6_{0,6})$	$(8_{0,8}-7_{0,7})$	$(12_{0,12}-11_{0,11})$
1	−17.3,	−10.4	12.14	9.00	5.25	2.47	0.94	0.00
2	−13.6,	−2.8	6.40	4.93	2.92	1.39	0.55	0.00
3	−6.5,	−4.2	6.39	7.99	8.96	9.06	8.36	3.02
6	0.4,	2.1	4.41	6.05	7.42	8.37	8.81	6.28
7	4.8,	4.2	11.12	12.40	11.84	9.95	7.48	0.88
8	10.0,	6.2	7.30	6.05	4.03	2.22	1.01	0.01
9	12.0,	5.6	13.08	10.73	7.11	3.85	1.73	0.01

Note. Integrated intensities of the $HOCO^+$ transitions produced by CASSIS fitting for hexagonal pixels closest to the GMCs. Results are shown only for GMCs with $HOCO^+$ detection.

The CO_2 ice fractional abundances near the center of NGC 253 (rectangular regions 2 and 3) are lower than in regions 4 and 5 by about an order of magnitude or more. Away from the center, the CO_2 ice fractional abundances are similar to those of the Milky Way ISM of $\sim 10^{-6}$–10^{-5} (Boonman et al. 2003), which are also consistent with the fractional abundances of CO_2 ice in our chemical model. Therefore, the CO_2 ice abundances decrease toward the center of NGC 253, deviating from the Milky Way value. We note that, if we use a higher dust temperature, we would derive lower H_2 column densities than those shown in Figure 4. Subsequently, the fractional abundance estimate would increase. Although warm dust does not fully explain the large difference in the derived fractional abundances between the outer part (rectangular regions 4 and 5) and center (rectangular regions 2 and 3) of the CMZ, this uncertainty should be considered in the interpretation of the data.

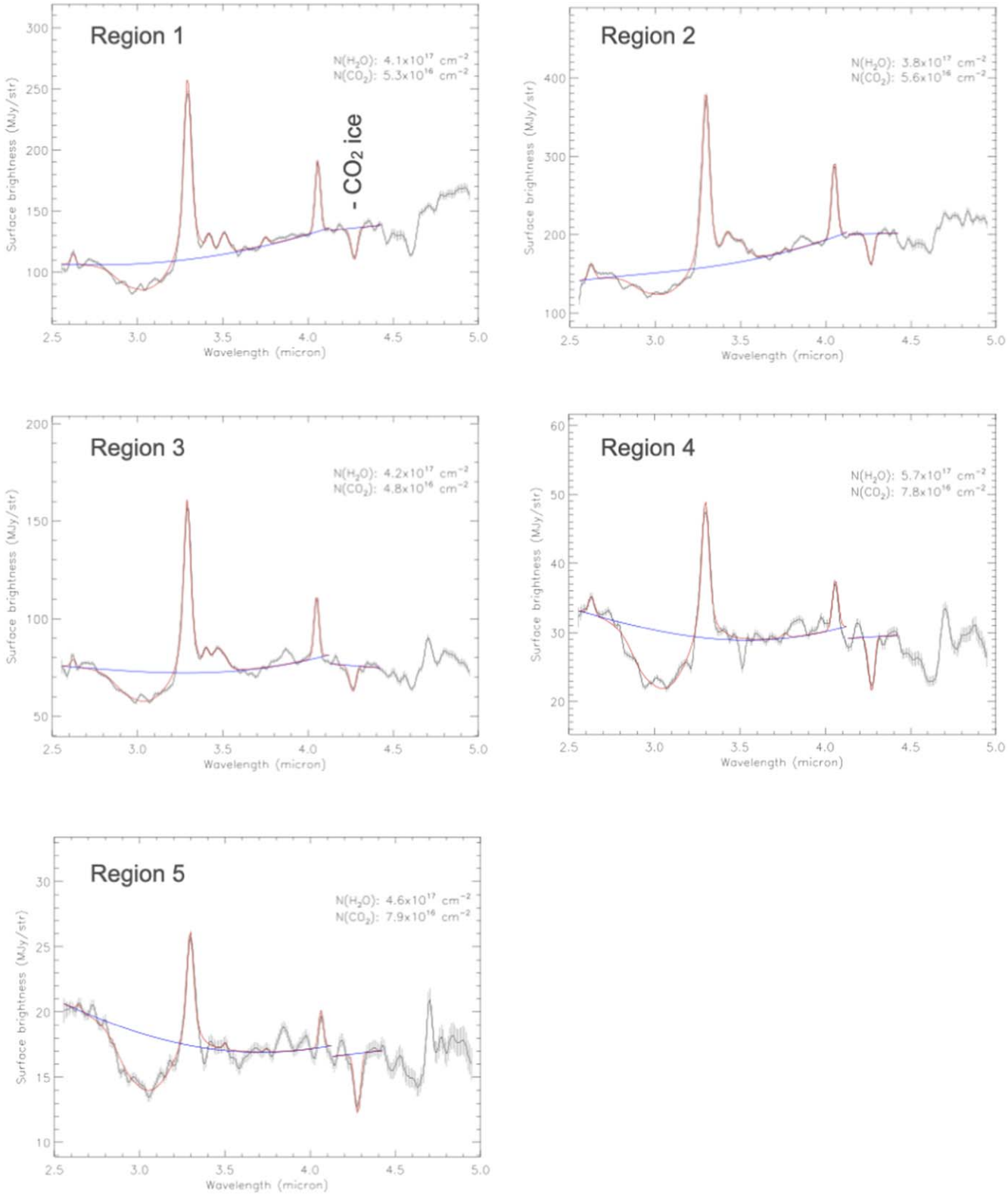

Figure 9. AKARI spectra for the regions used in our analysis. As in Figure 1 of Yamagishi et al. (2015), the blue curve represents the best-fit continuum emission while the red curve shows the overall spectral profiles.

If the CO_2 ice fractional abundance is indeed lower in the center than at the outer CMZ, one of the possible factors that may contribute to this suppression is photodissociation, either directly by UV photons or cosmic-ray-induced UV photons. Because of the high star formation rate in the rectangular regions 2 and 3, strong photodissociation is expected (Meier et al. 2015).

Warm dust can also lower the ice abundance of CO_2 through desorbing CO_2 ice into the gas phase, or desorbing the precursors of CO_2 ice. Desorption of many CO_2 precursors can

Table 3
GMC Positions

ID	R.A. (ICRS) $00^h47^m-^s$	Decl. (ICRS) $-25°17'-''$
1	32.02	28.2
2	32.28	20.2
3	32.81	21.6
4	32.97	20.0
5	33.21	17.4
6	33.33	15.8
7	33.64	13.3
8	34.02	11.4
9	34.17	12.3
10	34.24	7.8

Note. The modified coordinates of GMC positions of Leroy et al. (2015) were provided by A. K. Leroy (private communication).

take place with lower dust temperatures than the desorption of CO_2 itself. CO_2 ice is thought to be formed through (Minissale et al. 2013)

$$CO + OH \longrightarrow CO_2 + H, \quad (2)$$

$$CO + O \longrightarrow CO_2, \quad (3)$$

and possibly (Minissale et al. 2015)

$$H_2CO + O \longrightarrow CO_2 + H_2. \quad (4)$$

Some of these reactants have lower binding energies than $CO_2(E_b(CO_2) \sim 3000$ K, $E_b(CO) \sim 1300$ K, and $E_b(O) \sim 1600$ K (Wakelam et al. 2017; Minissale et al. 2022).[24] Higher dust temperatures increase the desorption rates of ice species, and species with lower binding energies can desorb with lower dust temperatures (35–50 K for CO, ∼50 K for O, and ∼80 K for CO_2; Minissale et al. 2022). If the desorption rate of any of these reactants is faster than the reaction rate to form CO_2 there would be less abundances of CO_2 ice. Although the mass of warm or hot dust is smaller than that of cold dust, these warm/hot components are likely concentrated in rectangular regions 2 and 3 in Figure 7 where the star formation is active. This can explain the suppression of ice in these regions as well as the low $HOCO^+$ fractional abundances in GMCs 4 and 5 (see Figure 2(f)).

Cosmic rays could also contribute to ice desorption. We argued in Section 5 that cosmic-ray-induced desorption is likely negligible, but its effect could possibly be enhanced in NGC 253. Hasegawa & Herbst (1993) estimated that the maximum dust temperature due to the cosmic-ray heating of the dust is 70 K, but this temperature can be different for the case of NGC 253, where some dust is already warm. With a higher maximum dust temperature, the evaporation rate of ice species can be enhanced (e.g., Kalvāns & Kalnin 2020). This dependence of desorption due to cosmic-ray heating on the dust temperature should be further explored with theoretical studies.

Variations of the CO_2 ice abundance can be also caused by the initial ice composition. For example, the ice may be rich in atomic or molecular hydrogen. If the ice is abundant in atomic H, frequent hydrogenation reactions can occur, and species such as water, CH_4, NH_3, and CH_3OH may be abundant. On the other hand, if atomic H is deficient, CO_2 formation may be a more dominant route of destroying CO ice than CH_3OH formation. Although it is difficult to assess how much the ice compositions differ between Galactic star-forming regions and the NGC 253 CMZ, we note that this is another factor that could affect the overall chemistry.

6.4. Ice and Gas-phase Chemistry in NGC 253

We find that the gas-phase fractional abundance of CO_2 can be $\sim(1–20) \times 10^{-7}$ in GMCs 1, 2, 8, and 9 (Section 6.2), and the ice fractional abundance is $\sim 2 \times 10^{-6}$ around GMC 1 (rectangular region 5 in Figure 7). This means that there is a process sublimating a large fraction of CO_2 ice into the gas phase in these GMCs.

One possible CO_2 sublimation mechanism is a hydrodynamical shock. Chemical models have shown that shocks can sputter ice because some gas particles have enough kinetic energy to desorb ice (Jiménez-Serra et al. 2008; Viti et al. 2011; Flower & Pineau des Forêts 2012). We also note that shock sublimation occurs even when the dust temperature is low, because energy is provided by the gas. When the shock velocity is higher than 20 km s^{-1}, ice sputtering is efficient enough to desorb a large fraction of ice (Harada et al. 2015). Ubiquitous methanol emission is likely attributed to shock sublimation in the Milky Way's Galactic Center (Menten et al. 2009), and this type of ice sublimation likely occurs also in NGC 253 with frequent shocks (Meier et al. 2015). Locations with enhanced $HOCO^+$ abundances are considered as intersections of different orbits. As shown in Figure 1, bar orbits (x_1 orbits) and inner orbits (x_2 orbits) intersect at the northeast and southwest parts of the CMZ, near GMCs 1, 8, 9, and 10. Shocks at GMCs 1, 2, 7, 8, 9, and 10 have been suggested by the detection of Class I methanol masers (Humire et al. 2022), and some other molecular tracers of shocks (K.-Y. Huang et al. 2022, in preparation). Because these regions are located at intersections of different orbits (bar and nuclear ring; see Sorai et al. 2000; Das et al. 2001; Levy et al. 2022, for dynamical modeling), shocks due to cloud collisions are not surprising.

If the shock scenario is correct, ice sputtering of other species in addition to CO_2 should be taking place. The methanol enhancement shown in Section 3 is one example supporting this scenario. Water is another species abundant in ice, and ice sputtering should increase its gas-phase abundance. From the H_2O/CO_2 ratio of ∼7 in ice (Yamagishi et al. 2015) and our estimated gas-phase fractional abundance of CO_2 of $(1–20) \times 10^{-7}$, the gas-phase water abundances in shocked regions must be $\sim(0.7–14) \times 10^{-6}$. This estimate assumes that the same fraction of CO_2 and H_2O ice is sublimated, and does not consider the higher desorption energy of water compared with CO_2. It also assumes that gas-phase reactions subsequent to sputtering do not change the CO_2H_2O ratio. Liu et al. (2017) derived fractional abundances of gas-phase water to be $\sim 10^{-7}$ from Herschel HIFI/PACS/SPIRE data using multiple transitions of water in analysis with all data convolved to 40″ at the center of NGC 253. This value may be locally higher in shocked regions. However, it is impossible to confirm it without spatially resolving shocked regions and nuclear starburst regions with higher-angular-resolution (<10″) observations.

[24] Note that the binding energy is not the temperature where desorption takes place. The effects of desorption appear when the desorption rate becomes significant enough compared with the accretion rate. There is also an additional complication caused by the ice composition. For example, even if a species has a low binding energy, it may not desorb if it is buried in the ice of another species with a higher binding energy.

Another possible CO_2 sublimation mechanism is thermal desorption. We do not know the distribution of the dust temperature due to a lack of high-angular-resolution data at the wavelengths of the peak blackbody radiation intensity ($\sim$10–100 μm for 30–300 K). Yet, we do know that the most active star formation takes place around GMCs 3–5 from radio recombination lines and 3 mm continuum data (Bendo et al. 2015; Harada et al. 2021). If the hot/warm dust components are concentrated in GMCs 3–5, it is unlikely that thermal desorption already takes place at GMCs 1 and 9. Therefore, thermal desorption unlikely contributes to the sublimation of CO_2 in GMCs 1, 2, 8, and 9. However, it is quite possible that thermal desorption occurs around GMCs 3–5 due to the high dust temperature.

Another mechanism which can sublimate CO_2 is cosmic-ray-induced desorption, as described in Section 6.3. We argued that this desorption mechanism is unlikely unless the dust is warm so that the maximum dust temperature achieved from the cosmic-ray heating of dust becomes significantly larger than 70 K. Without high star formation rates in GMCs 1 and 9, it is unlikely that the dust is already warm.

For the reasons above, we conclude that shocks are the most likely scenario driving the CO_2 evaporation. Yet, to constrain the ice fractional abundances better, high-angular-resolution observations at infrared wavelengths, e.g., from JWST, are crucial.

7. Summary

In this paper, we analysed the abundances of $HOCO^+$, the protonated form of CO_2, in the CMZ of the starburst galaxy NGC 253, and discussed its relationship with the gas- and ice-phase CO_2. Below is a summary of our findings.

1. The distribution of $HOCO^+$ shows clear enhancements at the locations of *the* x_1 and x_2 orbital intersections where shocks are expected. This distribution is similar to that of methanol but is different from that of $H^{13}CO^+$. There are two formation routes of $HOCO^+$; one is the ion-neutral reaction $HCO^+ + OH$ and the other is the protonation of CO_2. If the former route is dominant, the $HOCO^+$ distribution should be similar to that of HCO^+, while the latter route should cause similarity with the CH_3OH distribution. Therefore, $HOCO^+$ is likely produced through the protonation of CO_2.
2. We derive $HOCO^+$ column densities across the CMZ using CASSIS, from which we also obtain its fractional abundances using the total H_2 column densities estimated from the dust emission. We find $HOCO^+$ fractional abundances as high as $\sim 2 \times 10^{-9}$, which are similar to those observed in the Galactic center, but orders of magnitude higher than those reported in Galactic spiral-arm molecular clouds.
3. From the results of chemical modeling and the values of the cosmic-ray ionization rates derived from previous ALCHEMI works, we estimate that the gaseous $HOCO^+/CO_2$ ratio is likely 10^{-3}–10^{-2}. This ratio suggests that the gas-phase CO_2 fractional abundances are $(1\text{–}20) \times 10^{-7}$ at the peaks of $HOCO^+$ emission.
4. We also estimate fractional abundances of CO_2 ice from their column densities in the literature. The ice fractional abundance at the $HOCO^+$ peak is similar to the value in the Galactic interstellar medium (10^{-6}–10^{-5}), but is lower ($\sim(1\text{–}3) \times 10^{-7}$) near the NGC 253 galactic center.
5. The increased gaseous and ice fractional abundances of CO_2 at the outer CMZ of NGC 253 imply that a large fraction of ice is sublimated. Because of the association of these locations with the evidence of shocks, we propose that this efficient sublimation is attributed to shock-induced sputtering.

High-spatial-resolution observations of molecular emission in external galaxies, such as those performed by the ALCHEMI survey toward the central regions of the starburst galaxy NGC 253 with ALMA, have greatly improved our understanding of gas-phase abundances and will continue to do so. Now, complementary observations of ice at high angular resolutions with the JWST are required to obtain a complete picture of the chemical processes in starburst galaxies.

We thank the anonymous referee for constructive comments. N.H. thanks Hideko Nomura for the helpful discussion on CO_2 transitions at infrared wavelengths, and Kotomi Taniguchi for the initial help using CASSIS. This paper makes use of the following ALMA data: ADS/JAO.ALMA#2017.1.00161.L, ADS/JAO.ALMA#2018.1.00162.S, ADS/JAO.ALMA#2018.1.01321.S. ALMA is a partnership of ESO (representing its member states), NSF (USA) and NINS (Japan), together with NRC (Canada), MOST and ASIAA (Taiwan), and KASI (Republic of Korea), in cooperation with the Republic of Chile. The National Radio Astronomy Observatory is a facility of the National Science Foundation operated under cooperative agreement by Associated Universities, Inc. The Joint ALMA Observatory is operated by ESO, AUI/NRAO and NAOJ. Data analysis was in part carried out on the Multi-wavelength Data Analysis System operated by the Astronomy Data Center (ADC), National Astronomical Observatory of Japan. N.H. acknowledges support from JSPS KAKENHI grant No. JP21K03634. V.M.R. has received support from the Comunidad de Madrid through the Atracción de Talento Investigador Modalidad 1 (Doctores con experiencia) grant (COOL:Cosmic Origins of Life; 2019-T1/TIC-5379), and the Ayuda RYC2020-029387-I funded by MCIN/AEI/10.13039/501100011033. L.C. has received partial support from the Spanish State Research Agency (AEI; project number PID2019-105552RB-C41). K. N. acknowledges support from JSPS KAKENHI grant No. 19K03937. P.H. is a member of and received financial support for this research from the International Max Planck Research School (IMPRS) for Astronomy and Astrophysics at the Universities of Bonn and Cologne. K.S. is supported by the grant MOST 111-2112-M-001-039 from the Ministry of Science and Technology, Taiwan. This research has made use of the NASA/IPAC Extragalactic Database (NED), which is funded by the National Aeronautics and Space Administration and operated by the California Institute of Technology.

Facility: ALMA.

Software: Astropy (Astropy Collaboration et al. 2013, 2018), CASA (McMullin et al. 2007), CASSIS (Vastel et al. 2015), Nautilus (Ruaud et al. 2016).

Appendix A
CASSIS Fitting Parameters

CASSIS constrains parameters such as the column density, line velocity, line width (FWHM), excitation temperatures, and source sizes by fitting the spectra. We used the MCMC algorithm provided by CASSIS to derive these parameters. We used the transitions in the spectra, as shown in the upper half of Table 1. When using the MCMC method, users provide acceptable ranges of these parameters as well as initial guesses. We used the column-density range of $[10^{12}, 10^{16}]$ cm^{-2} with an initial guess of 10^{14} cm^{-2}, the excitation temperature range [5,50] K with an initial guess of 6 K, and the velocity range $[v_{\rm CO}-30, v_{\rm CO}+30.]$ km s^{-1}, where $v_{\rm CO}$ is the velocity obtained from the moment 1 image of CO(1-0), which is also used for the initial guess. The range of FWHM we used is [σ_V -20.,90.] km s^{-1} with an initial guess of σ_V, where σ_V is the velocity dispersion of the CO(1-0) image.[25] We note that the line width of $HOCO^+$ is significantly different from that of CO(1-0), and this range of FWHM is simply determined by running CASSIS multiple times and checking the range to produce a reasonable fit.

Uncertainties from the CASSIS fit are reasonably small for most cases. Figure 8 (left) shows that the errors of the column densities are around 10% for most cases, and ∼20%–30% for a small fraction of pixels with low signal-to-noise ratios. The uncertainties in the excitation temperatures are within 0.5 K for most pixels, with a maximum of 3 K (Figure 8, right).

There are also other sources of uncertainties, in addition to the spectral fitting. For example, the $HOCO^+$ column densities derived with the spectroscopic constants from the Jet Propulsion Laboratory (JPL[26]) would yield up to a factor of 2 larger values compared with ones from CDMS. Although this is a large factor, the use of different spectroscopic constants changes the results uniformly within the field of view. There are also observational uncertainties of up to 15% (Martín et al. 2021). These uncertainties will not change our main conclusions.

The $HOCO^+$ transitions are optically thin even where the column densities are high. CASSIS does not provide the optical depths, but we also ran MADCUBA (Martín et al. 2019), a similar spectral fitting software, to obtain optical depths. The optical depths are <0.1 for positions that we checked, which have high intensities of $HOCO^+$.

The modeled intensities with CASSIS for pixels that are closest to each GMC position are shown in Table 2 if a $HOCO^+$ transition for a GMC is detected.

Appendix B
Ice Data from AKARI

Here we summarize the analyses of Yamagishi et al. (2015), and present spectra for the regions used in our analysis. The observed wavelength range is about 2.5–5.0 μm. Within this range, CO_2 ice, H_2O ice, Brα, and PAH 3.3 μm features were detected in addition to the continuum. The CO_2 ice features at 4.27 μm are fit using the data range 4.1–4.4 μm as there is only this narrow ice feature in this wavelength range. Because the ice composition changes the spectral shape, multiple ice compositions were tested to best fit the spectra. Consequently, an ice composition of H_2O:CH_3OH:CO_2= 9: 1: 2 was used in the final analysis.

Figure 9 shows the spectra used to derive the CO_2 ice column densities shown in Figure 7. Note that our Regions 1–5 correspond to IDs 47–51 in Table 3 of Yamagishi et al. (2015).

Appendix C
GMC Positions

As already noted by Humire et al. (2022) and Behrens et al. (2022), the GMC nomenclature was adopted from Leroy et al. (2015), but with modified positions. How these modifications are made is explained in Behrens et al. (2022). These positions are shown in Table 3.

Appendix D
The Archival CO(2-1) Image

The large-scale CO(2-1) image of NGC 253 shown in Figure 1 was taken from the ALMA archive (project code #2018.1.01321.S). These data were obtained from a configuration consisting of the 7 m array complemented by the total power antenna. Pipeline-reduced image cubes (QA2 products) for the 7 m array and total power single-dish data were combined with the CASA command `feather`. This image was shown to indicate the rough positions of the x_1 and x_2 orbits only. We expect that the PI team will present the data with better imaging quality and scientific analysis.

ORCID iDs

Nanase Harada https://orcid.org/0000-0002-6824-6627
Sergio Martín https://orcid.org/0000-0001-9281-2919
Jeffrey G. Mangum https://orcid.org/0000-0003-1183-9293
Kazushi Sakamoto https://orcid.org/0000-0001-5187-2288
Sebastien Muller https://orcid.org/0000-0002-9931-1313
Víctor M. Rivilla https://orcid.org/0000-0002-2887-5859
Christian Henkel https://orcid.org/0000-0002-7495-4005
David S. Meier https://orcid.org/0000-0001-9436-9471
Laura Colzi https://orcid.org/0000-0001-8064-6394
Mitsuyoshi Yamagishi https://orcid.org/0000-0002-6385-8093
Kunihiko Tanaka https://orcid.org/0000-0001-8153-1986
Kouichiro Nakanishi https://orcid.org/0000-0002-6939-0372
Rubén Herrero-Illana https://orcid.org/0000-0002-7758-8717
Yuki Yoshimura https://orcid.org/0000-0002-1413-1963
P. K. Humire https://orcid.org/0000-0003-3537-4849
Rebeca Aladro https://orcid.org/0000-0002-1316-1343
Paul P. van der Werf https://orcid.org/0000-0001-5434-5942
Kimberly L. Emig https://orcid.org/0000-0001-6527-6954

References

Agúndez, M., Cernicharo, J., de Vicente, P., et al. 2015, A&A, 579, L10
Aladro, R., Martín, S., Riquelme, D., et al. 2015, A&A, 579, A101
Armijos-Abendaño, J., Martín-Pintado, J., Requena-Torres, M. A., Martín, S., & Rodríguez-Franco, A. 2015, MNRAS, 446, 3842
Astropy Collaboration, Price-Whelan, A. M., Sipőcz, B. M., et al. 2018, AJ, 156, 123
Astropy Collaboration, Robitaille, T. P., Tollerud, E. J., et al. 2013, A&A, 558, A33

[25] The relationship between the FWHM and the standard deviation of a Gaussian distribution is usually described as $FWHM \sim 2.355\sigma_V$. In our case, the line width of $HOCO^+$ is much smaller than that of CO(1-0), and the initial guess of σ_V for the FWHM of $HOCO^+$ is still a reasonable one.
[26] https://spec.jpl.nasa.gov/

Athanassoula, E. 1992, MNRAS, 259, 345
Behrens, E., Mangum, J. G., Holdship, J., et al. 2022, ApJ, in press
Bendo, G. J., Beswick, R. J., D'Cruze, M. J., et al. 2015, MNRAS, 450, L80
Bizzocchi, L., Lattanzi, V., Laas, J., et al. 2017, A&A, 602, A34
Bolatto, A. D., Warren, S. R., Leroy, A. K., et al. 2013, Natur, 499, 450
Boonman, A. M. S., van Dishoeck, E. F., Lahuis, F., & Doty, S. D. 2003, A&A, 399, 1063
Cohen, D. P., Turner, J. L., & Consiglio, S. M. 2020, MNRAS, 493, 627
Dale, D. A., Cohen, S. A., Johnson, L. C., et al. 2009, ApJ, 703, 517
Das, M., Anantharamaiah, K. R., & Yun, M. S. 2001, ApJ, 549, 896
Defrees, D. J., Loew, G. H., & McLean, A. D. 1982, ApJ, 254, 405
Flower, D. R., & Pineau des Forêts, G. 2012, MNRAS, 421, 2786
Fontani, F., Vagnoli, A., Padovani, M., et al. 2018, MNRAS, 481, 79
García-Burillo, S., Martín-Pintado, J., Fuente, A., & Neri, R. 2000, A&A, 355, 499
Garrod, R. T., & Pauly, T. 2011, ApJ, 735, 15
Garrod, R. T., Wakelam, V., & Herbst, E. 2007, A&A, 467, 1103
Haasler, D., Rivilla, V. M., Martín, S., et al. 2022, A&A, 659, A158
Harada, N., Martín, S., Mangum, J. G., et al. 2021, ApJ, 923, 24
Harada, N., Riquelme, D., Viti, S., et al. 2015, A&A, 584, A102
Harada, N., Sakamoto, K., Martín, S., et al. 2019, ApJ, 884, 100
Hasegawa, T. I., & Herbst, E. 1993, MNRAS, 261, 83
Herbst, E., Green, S., Thaddeus, P., & Klemperer, W. 1977, ApJ, 215, 503
Hildebrand, R. H. 1983, QJRAS, 24, 267
Holdship, J., Mangum, J. G., Viti, S., et al. 2022, ApJ, 931, 89
Holdship, J., Viti, S., Martín, S., et al. 2021, A&A, 654, A55
Humire, P. K., Henkel, C., Hernández-Gómez, A., et al. 2022, A&A, 663, A33
Jiménez-Serra, I., Caselli, P., Martín-Pintado, J., & Hartquist, T. W. 2008, A&A, 482, 549
Kalvāns, J., & Kalnin, J. R. 2020, A&A, 633, A97
Kim, W.-T., Seo, W.-Y., & Kim, Y. 2012, ApJ, 758, 14
Krieger, N., Bolatto, A. D., Walter, F., et al. 2019, ApJ, 881, 43
Lahuis, F., Spoon, H. W. W., Tielens, A. G. G. M., et al. 2007, ApJ, 659, 296
Le Petit, F., Nehmé, C., Le Bourlot, J., & Roueff, E. 2006, ApJS, 164, 506
Leroy, A. K., Bolatto, A. D., Ostriker, E. C., et al. 2015, ApJ, 801, 25
Levy, R. C., Bolatto, A. D., Leroy, A. K., et al. 2022, ApJ, 935, 19
Liu, L., Weiß, A., Perez-Beaupuits, J. P., et al. 2017, ApJ, 846, 5
LVL team 2009, Spitzer Local Volume Legacy Survey
Majumdar, L., Gratier, P., Wakelam, V., et al. 2018, MNRAS, 477, 525
Mangum, J. G., Ginsburg, A. G., Henkel, C., et al. 2019, ApJ, 871, 170
Martín, S., Mangum, J. G., Harada, N., et al. 2021, A&A, 656, A46
Martín, S., Martín-Pintado, J., Blanco-Sánchez, C., et al. 2019, A&A, 631, A159
Martín, S., Mauersberger, R., Martín-Pintado, J., Henkel, C., & García-Burillo, S. 2006, ApJS, 164, 450
McMullin, J. P., Waters, B., Schiebel, D., Young, W., & Golap, K. 2007, in ASP Conf. Ser., 376, Astronomical Data Analysis Software and Systems XVI, ed. R. A. Shaw, F. Hill, & D. J. Bell (San Francisco, CA: ASP), 127
Meier, D. S., & Turner, J. L. 2005, ApJ, 618, 259
Meier, D. S., Walter, F., Bolatto, A. D., et al. 2015, ApJ, 801, 63
Menten, K. M., Wilson, R. W., Leurini, S., & Schilke, P. 2009, ApJ, 692, 47
Minh, Y. C., Brewer, M. K., Irvine, W. M., Friberg, P., & Johansson, L. E. B. 1991, A&A, 244, 470
Minh, Y. C., Irvine, W. M., & Ziurys, L. M. 1988, ApJ, 334, 175
Minissale, M., Aikawa, Y., Bergin, E., et al. 2022, ESC, 3, 597
Minissale, M., Congiu, E., Manicò, G., Pirronello, V., & Dulieu, F. 2013, A&A, 559, A49
Minissale, M., Loison, J. C., Baouche, S., et al. 2015, A&A, 577, A2
Müller, H. S. P., Schlöder, F., Stutzki, J., & Winnewisser, G. 2005, JMoSt, 742, 215
Müller, H. S. P., Thorwirth, S., Roth, D. A., & Winnewisser, G. 2001, A&A, 370, L49
Muller, S., Beelen, A., Black, J. H., et al. 2013, A&A, 551, A109
Müller-Sánchez, F., González-Martín, O., Fernández-Ontiveros, J. A., Acosta-Pulido, J. A., & Prieto, M. A. 2010, ApJ, 716, 1166
Öberg, K. I., Boogert, A. C. A., Pontoppidan, K. M., et al. 2011, ApJ, 740, 109
Öberg, K. I., Linnartz, H., Visser, R., & van Dishoeck, E. F. 2009a, ApJ, 693, 1209
Öberg, K. I., van Dishoeck, E. F., & Linnartz, H. 2009b, A&A, 496, 281
Pérez-Beaupuits, J. P., Güsten, R., Harris, A., et al. 2018, ApJ, 860, 23
Rekola, R., Richer, M. G., McCall, M. L., et al. 2005, MNRAS, 361, 330
Rico-Villas, F., Martín-Pintado, J., González-Alfonso, E., Martín, S., & Rivilla, V. M. 2020, MNRAS, 491, 4573
Rivilla, V. M., Martín-Pintado, J., Jiménez-Serra, I., et al. 2019, MNRAS, 483, L114
Ruaud, M., Wakelam, V., & Hersant, F. 2016, MNRAS, 459, 3756
Sakai, N., Sakai, T., Aikawa, Y., & Yamamoto, S. 2008, ApJ, 675, L89
Sakamoto, K., Ho, P. T. P., Iono, D., et al. 2006, ApJ, 636, 685
Sakamoto, K., Mao, R.-Q., Matsushita, S., et al. 2011, ApJ, 735, 19
Seo, W.-Y., & Kim, W.-T. 2013, ApJ, 769, 100
Sorai, K., Nakai, N., Kuno, N., Nishiyama, K., & Hasegawa, T. 2000, PASJ, 52, 785
Sormani, M. C., & Li, Z. 2020, MNRAS, 494, 6030
Thaddeus, P., Guelin, M., & Linke, R. A. 1981, ApJL, 246, L41
Turner, B. E., Terzieva, R., & Herbst, E. 1999, ApJ, 518, 699
Turner, J. L., & Ho, P. T. P. 1985, ApJ, 299, L77
Vastel, C., Bottinelli, S., Caux, E., Glorian, J. M., & Boiziot, M. 2015, in SF2A-2015: Proc. Annual Meeting of the French Society of Astronomy and Astrophysics, ed. F. Martins et al., 313
Vastel, C., Ceccarelli, C., Lefloch, B., & Bachiller, R. 2016, A&A, 591, L2
Viti, S., Jimenez-Serra, I., Yates, J. A., et al. 2011, ApJL, 740, L3
Wakelam, V., Loison, J. C., Mereau, R., & Ruaud, M. 2017, MolAs, 6, 22
Yamagishi, M., Kaneda, H., Ishihara, D., et al. 2015, ApJ, 807, 29